

Crystal Growth and basic transport and magnetic properties of MnBi_2Te_4

Poonam Rani¹, Ankush Saxena^{1,2}, Rabia Sultana^{1,2}, Vipin Nagpal³, S.S. Islam⁴, S. Patnaik³, and V.P.S. Awana^{1,2,*}

¹National Physical Laboratory (CSIR), Dr. K. S. Krishnan Road, New Delhi-110012, India

²Academy of Scientific and Innovative Research (AcSIR), Ghaziabad-201002, India

³School of Physical Sciences, Jawaharlal Nehru University, New Delhi-110067, India

⁴Centre for Nanoscience and Nanotechnology, Jamia Millia Islamia New Delhi-110025, New Delhi, India

We report successful growth of magnetic topological insulator (MTI) MnBi_2Te_4 . Depending, upon the heating schedule the phase formation in terms of various $\text{Bi}_2\text{Te}_3 + \text{MnTe}$ structures viz. MnBi_2Te_4 , MnBi_4Te_7 , $\text{MnBi}_6\text{Te}_{10}$ and MnTe are seen in powder X-ray diffraction of crushed resultant crystals. The heating schedule basically deals with growth of the crystal from melt at 900°C and very slow cooling (1°C/hr) to around 600°C with 24 hours hold time, followed by cooling to room temperature. Our detailed, PXRD Reitveld analysis showed that the resultant crystal is dominated by MnBi_4Te_7 , $\text{MnBi}_6\text{Te}_{10}$ phases along with some MnTe content. The transport measurements showed a step like behavior at around 150K followed by cusp like structure in resistivity at around 20K (T_p) due reported anti-ferromagnetic ordering of Mn. Both the resistivity transitions are seen clearly in dR/dT measurements at 150K and 20K respectively. The 20K transition of the compound is also seen in magnetic susceptibility. Low temperature (5K) magneto-resistance (MR) in applied field of up to 6 Tesla exhibited -ve MR below 3 Tesla and +ve for higher fields. Also, seen are steps in MR below one Tesla. The studied MnBi_2Te_4 MTI crystal could be a possible candidate for Quantum Anomalous Hall (QAH) effect.

Key Words: Magnetic Topological Insulator, Crystal Growth, Structural Details, Surface Morphology and Electrical Transport

PACS: 74.70.Dd, 74.62.Fj, 74.25.F-

***Corresponding Author**

Dr. V. P. S. Awana: E-mail: awana@nplindia.org

Ph. +91-11-45609357, Fax +91-11-45609310

Homepage: awanavps.webs.com

Topological Insulators (TIs) are dominating the quantum condensed matter for over a decade by now [1-3]. In this direction, one of the most happening new advancement had been

the magnetic topological insulators (MTIs). In case of MTIs, a magnetic layer or element is inserted among the running TI unit cells of bulk 3D topological insulators such as 3d metal doped Bi_2Se_3 , Bi_2Te_3 and Sb_2Te_3 [4-6]. The insertion of magnetic layer along running 3D bulk topological insulators shifts the Dirac position and thus alters the quantum transport properties of the parent system [8-10]. One of the most fascinating properties of the MTIs is the appearance of Quantum Anomalous Hall (QAH) effect [7-9].

QAH happens due to the finite Hall Voltage created due to magnetic polarization and spin-orbit coupling, while the external magnetic field is absent. QAH is found to be in integer multiple of e^2/h which is called Landau Level [9]. In principle, the inherent magnetism and topological electronic states are the necessary conditions for QAH. Though ultra thin films of TIs with enhanced surface area may exhibit QAH due to strong spin orbit coupling (SOC), but is a rare possibility and if at all the same takes place at ultra low temperatures [10]. Other possibility to realize QAH is to dope the 3D bulk topological material with transition metal elements viz. Co, Cr, Eu etc. [11, 12]. In this case as well because of randomly distributed 3d metal impurity to the realization of QAH is often difficult and if at all is at mK temperatures [10-13]. The best solution till date to observe QAH at higher temperatures is via the MTIs. A magnetic topological insulator having strong SOC exhibits quantized resistance and non-dissipative current at room temperature [14]. In case of MTIs, a 3d metal based magnetically ordered layer is inserted between the running 3D bulk topological insulator. An ideal example, being put forward by theoreticians [15-17] and very recently realized by experimentalists is MnBi_2Te_4 [18-20]. MnBi_2Te_4 can be formulated as Bi_2Te_3 and MnTe , here the former is the 3D bulk topological insulator and later the magnetically ordered layer being inserted in the periodic structure at van der Waals gaps [21]. MnBi_2Te_4 is the first 3D antiferromagnetic topological insulator [18-20, 22]. Interestingly, there are only scant reports on MnBi_2Te_4 , in particular the single crystals [22].

Keeping in view, the importance of QAH, the MTIs and the first 3D antiferromagnetic topological insulator, i.e. MnBi_2Te_4 , we report here the crystal growth and characterization of the same. Detailed, PXRD Reitveld analysis showed that the resultant crystal is dominated by MnBi_4Te_7 , $\text{MnBi}_6\text{Te}_{10}$ phases along with some MnTe content. Resistivity measurements exhibited two transitions at 150K and 20K. The studied MnBi_2Te_4 MTI crystal could be a possible good candidate for Quantum Anomalous Hall Effect (QAHE).

The constituent elements Mn, Bi and Te of better than 3N purity are weighed (1gram) in stoichiometric ratio and grind in a glove box filled with Argon. Proper care is taken to avoid the exposure of the material from air. After grinding the powder is converted into pallet, which is further sealed into a vacuum tube under the pressure of 10^{-5} mb. Now the sealed tube is held in

the electronically controlled furnace at high temperature. The temperature goes up to 900°C with heating rate of 120°C/hour. The temperature of furnace remains hold at 900°C for 12 Hour. Now the temperature starts to decrease at the rate of 1°C/Hour and goes down to 600°C. This temperature remains hold for 12 Hour followed by normal cooling to room temperature. The schematic of details of the heat treatment is given in Fig. 1 and the photograph of as grown crystal (MTI) is shown in Fig2. Powder X-ray diffraction pattern (PXRD) of the gently crushed part of crushed crystal is taken on Rigaku X-ray diffractometer in the range 10° to 80° of 2θ° at scan rate of 2°/min. Scanning Electron Microscope (SEM) make Bruker is used to visualize the morphology of the studied crystal. Raman spectrum of the crystal piece is taken on LabRam HR800-JY equipped with a laser source of 514 nm. The spectrum is taken in wave number range of 50 cm⁻¹ to 400 cm⁻¹. Resistivity versus temperature measurements are done on a Physical Property Measurement System (PPMS) in temperature range of 300 K down to 10 K on a close cycle refrigerator.

Fig. 3 shows the powder XRD (X-ray diffraction) pattern of the part of crushed MnBi₂Te₄ crystal being shown in Fig. 2. The full profile Reitveld analysis is carried out on the observed pattern. The PXRD pattern is similar to that as observed recently for MnBi₂Te₄ self flux grown crystals [23]. The main phase is found to be distorted MnBi₂Te₄ i.e., MnBi₆Te₁₀ (56%) with space group Space group R-3m and lattice parameters a = 4.0533(1) Å and c = 103.7673(1) Å. Followed by, MnBi₂Te₄ with lattice parameters a = 4.3882(1) Å and c = 42.7125(1) Å along with MnBi₄Te₇ having lattice parameters a = 4.3564(2) Å and c = 23.8227(4) Å. Also a minimal amount (~1%) of MnTe is also seen. There are some un-reacted lines not fitting with the main pattern and these belong to Bi₂Te₃. The Wyckoff and coordinate positions obtained from detailed multi phase Reitveld analysis for major phases i.e., MnBi₆Te₁₀ (56%), MnBi₂Te₄ (39%) and MnBi₄Te₇ (4%) are given in table 1. The situation is very similar to that as reported in ref. 23. The goodness of fitting parameters is $\chi^2 = 2.83$, which is reasonably good. The VISTA based software drawn unit cells for major MnBi₂Te₄ and MnBi₆Te₁₀ are given in Fig. 4. The c-parameter for the former is around 40 Å and for the later is above 100 Å. The general formula for these homologous series of compounds can be simplified as follows MnTe + nBi₂Te₃, with n = 1, 2, 3, as MnBi₂Te₄, MnBi₄Te₇ and MnBi₆Te₁₀. So, principally it depends upon the fact that after how many unit cells of Bi₂Te₃ an MnTe magnetic layer is inserted.

Fig.5 depicts the scanning electron microscope (SEM) picture of the surface of the as grown crystal at lower magnification. The slab like layered growth can be visualized. To further elaborate on the micro-structure of the studied crystal, the higher magnification picture is shown in Fig. 6, here the slab like uni-directional layered structure is clearly visible. We also did the

EDAX to know the composition of the crystal at various points on the micrograph. The resultant composition was although near stoichiometric for Bi and Te but less in Mn content.

The Raman spectrum of the as grown MnBi_2Te_4 taken at Laser wavelength of 514 nm is given in Fig. 7. A broad peak with three to four main shoulders is seen in the range of 50 to 200nm. We de-convoluted the main peak being at 120 nm consisting of 102 nm and 140 nm shoulders. The main peak at 120 nm is having maxim intensity and two others at lower and higher wave numbers show much less intensity. The general overall look of the Raman spectrum shown in Fig. 7 is similar to that as reported in ref. 23 for MnBi_2Te_4 .

The resistivity (ρ) versus temperature (T) plot for studied MnBi_2Te_4 crystal in temperature range of 300K down to 10K is shown in Fig. 8. The $\rho(T)$ behavior is metallic in nature with a step like change in slope at around 150K, followed by a small kink at around 20K. The 20K transition is very feeble and hence for more clarity is shown in inset of Fig.8. The 20K transition in $\rho(T)$ of MnBi_2Te_4 is reported earlier [15-18, 22] and is due to the Anti ferromagnetic ordering of Mn spins [18, 22] in MnTe layers of running Bi_2Te_3 3D topological insulator. To elaborate more on the transport behavior, the derivative of resistivity ($d\rho/dT$) is plotted against temperature (T) in Fig. 9. Here not only the 150K transition of metallic resistivity is seen, but the Mn magnetic ordering related 20K transition is also seen clearly. The expanded part of the $d\rho/dT$ versus T plot is shown in inset of Fig. 9. Summarily, the electrical transport measurements without applying magnetic field show two transitions at around 150K and 20K. Though, magnetic transition in rage of 20 to 30K is known to be due to Mn ordering [15-18, 22-25], the origin of 150K transition is on the other hand not clear as of now.

The magnetic moment (M) versus temperature plot in temperature range of 50 to 10K in both field cooled (FC) and Zero Field Cooled (ZFC) situations at 1000 Gauss for studied MnBi_2Te_4 is depicted in Fig. 10. It is clear from Fig. 10, that there is a clear anomaly at below 30K in $M(T)$ plot. The anomaly in magnetic susceptibility occurs nearly at the same temperature as being seen in transport measurements in Fig. 8 and 9, though at slightly higher temperature in $M(T)$ as the measurements are done under applied field of 1000Gauss.

Fig. 11 shows the magneto-resistance measurements done at 5K in applied magnetic field of up to 6 Tesla. The magneto-resistance decreases with increase in field of up to say one Tesla (H_1) and for higher fields starts increasing and becomes positive above 3 Tesla (H_2). Clearly, the magnetic ordering of Mn in MnTe layer of MnBi_2Te_4 has an effect on the magneto transport of the same. The expanded region (below H_1) of resistivity against magnetic field for the studied crystal is shown in inset of Fig.1. It is clear that initially the resistivity versus field plot is linear but starts showing step above say 0.5 Tesla, which are reminiscent of quantum transport.

Detailed experiments for observation of Quantum Anomalous Hall (QAH) effect are underway in the magnetic field regime of much less than H_1 in different protocols. In summary, the short communications reports the growth and basic physical properties of the magnetic topological insulator MnBi_2Te_4 .

Table 1: Crystal structure data and details of data refinement for the investigated phases of as grown MnBi_2Te_4 crystal

	Wyckoff	x	y	z
MnBi_2Te_4 (39%) Space group R-3m a = 4.3882(1) c = 42.7125(1)				
Bi1	6c	0	0	0.426(2)
Te1	6c	0	0	0.1443(9)
Te2	6c	0	0	0.2890(6)
Mn1	3a	0	0	0
MnBi_4Te_7 (4%) Space group P-3m1 a = 4.3564(2) c = 23.8227(4)				
Bi1	2d	1/3	2/3	0.0697(1)
Bi2	2d	1/3	2/3	0.2847(9)
Te1	1a	0	0	0
Te2	2d	2/3	1/3	0.1655(8)
Te3	2c	0	0	0.2841(3)
Te4	2d	2/3	1/3	0.4223(8)
Mn1	1b	0	0	1/2
$\text{MnBi}_6\text{Te}_{10}$ (56%) Space group R-3m a = 4.0533(1) c = 103.7673(1)				
Bi1	6c	0	0	0.2334(4)
Bi2	6c	0	0	0.2911(2)
Bi3	6c	0	0	0.47087(2)
Te1	6c	0	0	0.52615(2)
Te2	6c	0	0	0.11584(2)
Te3	6c	0	0	0.17621(3)
Te4	6c	0	0	0.34982(2)
Te5	6c	0	0	0.4096(5)
Mn1	3a	0	0	0

Figure Captions

Figure 1 Heat treatment schedule for the MnBi_2Te_4 crystals

Figure 2 Photograph of the MnBi_2Te_4 crystals

Figure 3 XRD of MnBi_2Te_4

Figure 4 Unit cells for MnBi_2Te_4 observed major phases (*124:39%, 1610:56%*)

Figure 5 SEM image of MnBi_2Te_4 at low magnification

Figure 6 SEM image of MnBi_2Te_4 at higher magnification, depicting clearly the layered growth.

Figure 7 Raman of MnBi_2Te_4

Figure 8 Resistivity versus temperature plot of MnBi_2Te_4 Crystal, inset shows the zoom part of same, marking the possible 20K magnetic ordering of Mn.

Figure 9 Derivative of resistivity versus temperature plot of MnBi_2Te_4 crystal, inset shows the zoom part of same, marking the 20K magnetic ordering of Mn

Figure 10 Magnetic moment (M) vs temperature (T) plot for MnBi_2Te_4 crystal in both Zero-Field-Cooled (ZFC) Field Cooled (FC) situations at 1000 Oe, possible AFM ordering temperature for MN at around 27K is marked as a dip in M(T) plot.

Figure 11 Magneto resistances versus field plot for MnBi_2Te_4 crystal in applied magnetic field of up to 6 Tesla, inset shows the resistivity versus field plot for the same in lower applied fields of up to one Tesla, marking the possible quantum steps.

References

1. C.L. Kane and E.J. Mele, *Physical Review Letters* **95**, 146802 (2005)
2. F.D.M. Haldane, *Phys. Rev. Lett.* **61**, 2015 (1988)
3. L. Fu, C.L. Kane and E.J. Mele, *Phys. Rev. Lett.* **98**, 106803 (2007)
4. Y.L. Chen, et al. *Science*, **325**, 178 (2009)
5. R. Sultana, P. Neha, R. Goyal, S. Patnaik and V.P.S. Awana, *J. Magn. Mag. Mater.* **428**, 213 (2017)
6. R. Sultana, G. Gurjar, S. Patnaik and V.P.S. Awana, *Mat. Res. Exp.* **5**, 046107 (2018)
7. C.-X. Liu, S.-C. Zhang and X.-L. Qi, *Annual Review of Condensed Matter* **7**, 301 (2016)
8. C.-Z. Chang, J. Zhang, X. Feng, J. Shen, Z. Zhang, M. Guo, L. Minghua, O. Kang and W.P. Yunbo, *Science* **340**, 6129 (2013)
9. M.Z. Hasan and C.L. Kane, *Rev. Mod. Phys.* **82**, 3045 (2010)
10. C.-Z. Chang, W.-W. Zhao, D.-Y. Kim, H.-J. Zhang, B.-A. Assaf, D. Heiman, S.-C. Zhang, C.-X. Liu, M.H.W. Chan, and J. S. Moodera, *Nature Materials*, **14**, 473 (2015).
11. X. Kou, L. He, M. Lang, Y. Fan, K. Wong, Y. Jiang, T. Nie, W. Jiang, P. Upadhyaya, Z. Xing, Y. Wang, F. Xiu, R. N. Schwartz, K. L. Wang, *Nano. Lett.* **13**, 4587 (2013)
12. M. Mogi, R. Yoshini, A. Tsukazaki, K. Yosuda, Y. Kozuka, K. S. Takahashi, M. Kawasaki, Y. Tokoura, *Appl. Phys. Lett.* **107**, 182401 (2015).
13. C.-Z. Chang, J. Zhang, X. Feng, J. Shen, Z. Zhang, M. Guo, K. Li, Y. Ou, P. Wei, L.-Wang, Z.-Q. Ji, Y. Feng, S. Ji, X. Chen, J.-F. Jia, X. Dai, Z. Fang, S.-C. Zhang, K. He, Y. Wang, L. Lu, X.-C. Ma, Q.-K. Xue, *Science*, **340**, 161 (2013)
14. M. M. Otrokov, T. V. Menshchikova, M. G. Vergniory, I. P. Rusinov, A.Y. Vyazovskaya, Y. M. Koroteev, G. Bihlmayer, A. Ernest, P. M. Echenique, A. Arnau, et al., *2D Materials* **4**, 025082 (2017).
15. M. M. Otrokov, I. I. Klimovskikh, H. Bentmann, A. Zeugner, Z. S. Aliev, S. Gass, A. U. Wolter, A. V. Koroleva, D. Estyunin, A. M. Shikin, et al., *arxiv.1809.07389* (2018)
16. D. Zhang, M. Shi, K. He, D. Xing, H. Zhang, J. Wang, *Phys. Rev. Lett.* **122**, 206401 (2019)
17. M. Otrokov, I. Rusinov, M. Blanco-rey, M. Hoffmann, A.Y. Vyazovskaya, S. Eremeev, A. Ernest, P. M. Echenique, A. Arnau, E. Chulkov, *Phys. Rev. Lett.* **122**, 107202 (2019).
18. J. Cui, M. Shi, H. Wang, F. Yu, T. Wu, X. Luo, J. Ying, X. Chen, *Phys. Rev. B.* **99**, 155125 (2019).

19. R. Visdal, H. Bentmann, T. Peixoto, A. Zeugner, S. Moser, C. Min, S. Schatz, K. Kissner, A. Unzelmann, C. Fornari et al., *arxiv.1903.11826* (2019).
20. Y. Gong, J. Guo, J. Li, K. Zhu, M. Liao, X. Liu, Q. Zhang, L. Gu, L. Tang, X. Feng, et al., *arxiv.1809.07926* (2018).
21. D. S. Lee, T.- H. Kim, C.- H. Park, C. –Y. Chung, Y. S. Lin, W. –S. Seo, H.- H. Park, *Cryst. Engg. Commun.* **15**, 5532 (2013).
22. J. Li, Y. Li, S. Du, Z. Wang, B. – L. Gu, S. – C. Zhang, K. He, W. Duan, Y. Xu, *Science Advances* , **5**, no. 6, *DOI:10.1126/sxciadv.aaw5685*
23. Z.S. Aliev, I.R. Amiraslanov, D. I. Nasonova, A. V. Shevelkov, N.A. Abdullayev, Z. A. Jahangirli, E. N. Orujlu, M. M. Otrokov, N. T. Mamedov, M. B. Babanly, E. V. Chulkov, *J. Alloys. & Comp.* **789**, 443 (2019).
24. J.Q. Yan, Q. Zhang, T.Heitmann, Z.L. Huang, W.D. Wu, D. Vaknin, B.C. Sales, N.R.J. McQueeney, *arXiv:1902.10110* (2019)
25. R.C. Vidal, A. Zeugner, J. I. Facio, R. Ray, M. H. Haghghi, A.U.B. Wolter, L.T.C. Bohorquez, F. Cagliaris, S. Moser, T. Figgemeier, T.R.F. Peixoto, H.B. Vasili, M. Valvidares, S. Jung, C. Cacho, A. Alfonsov, K. Mehlawat, V. Kataev, C. Hess, M. Richter, B. Buchner, J. van den Brink, M. Ruck, F. Reinert, H. Bentmann, A. Isaeva, *arXiv:1906.08394*

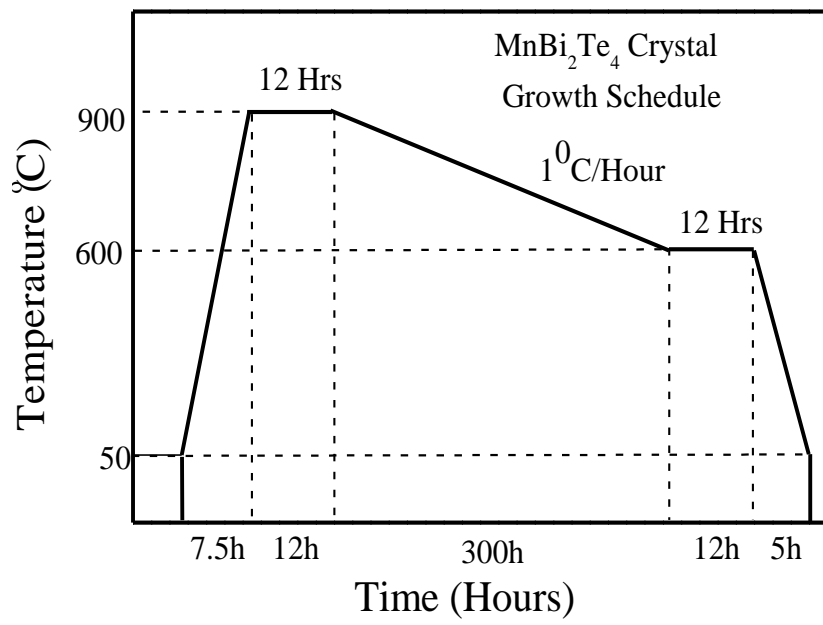


Fig. 1



Fig. 2

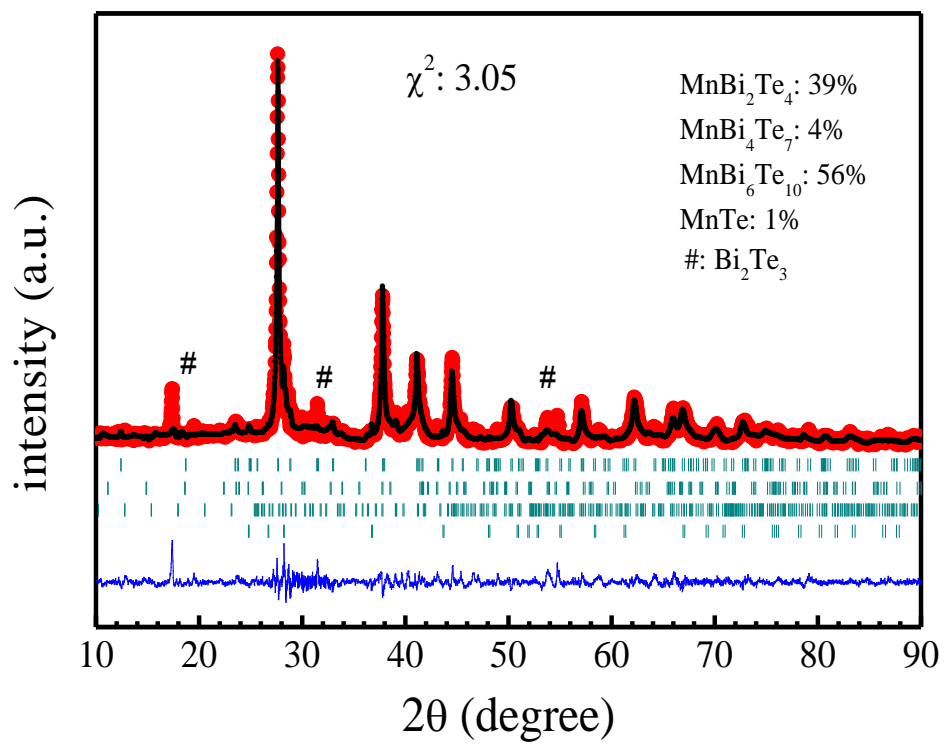


Fig. 3

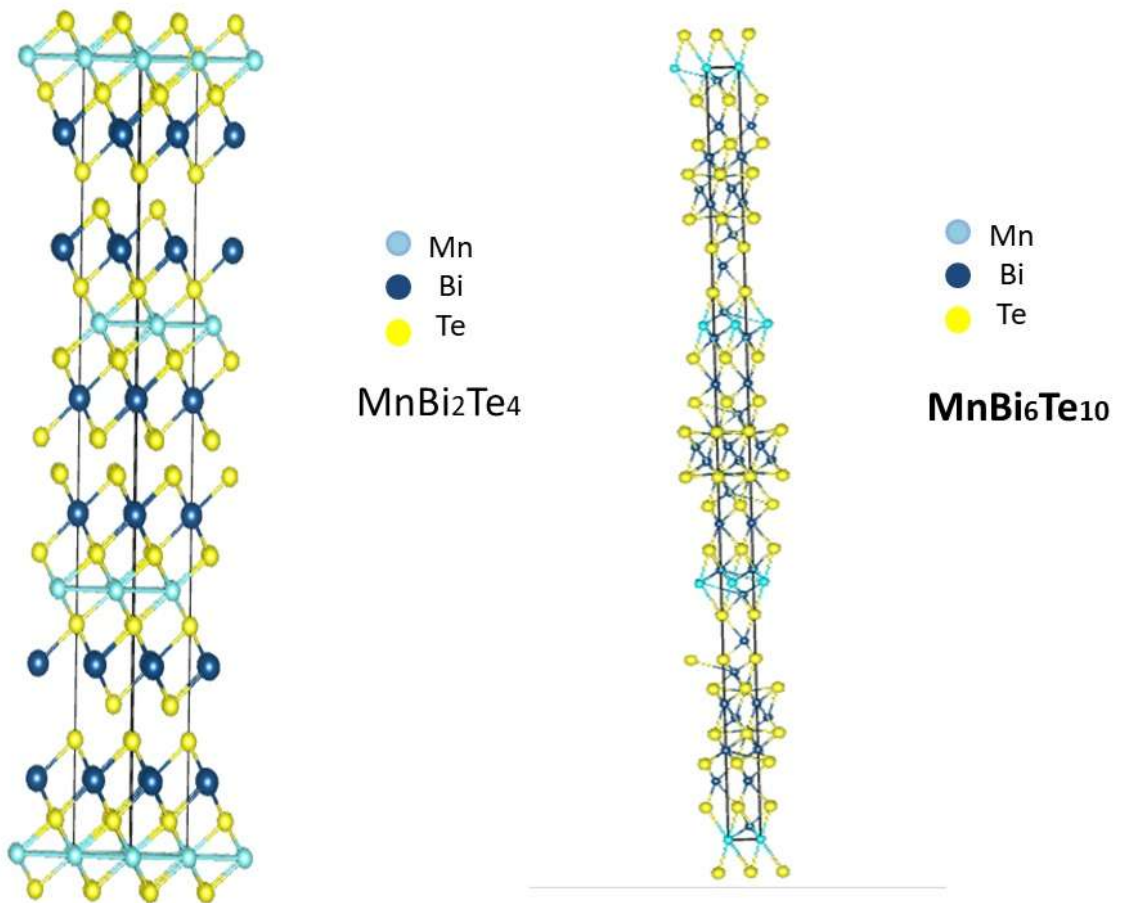


Fig. 4

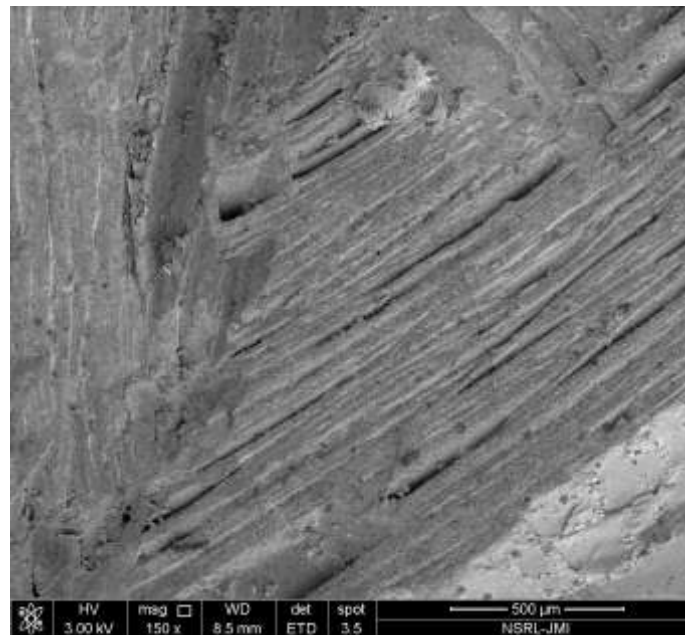


Fig. 5

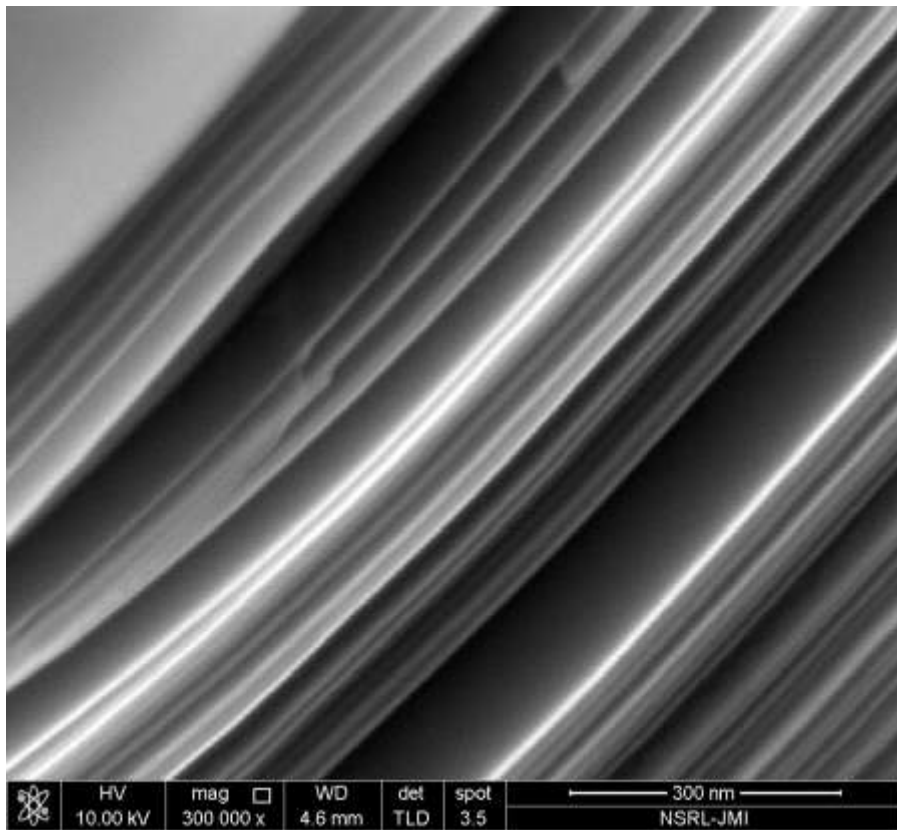


Fig. 6

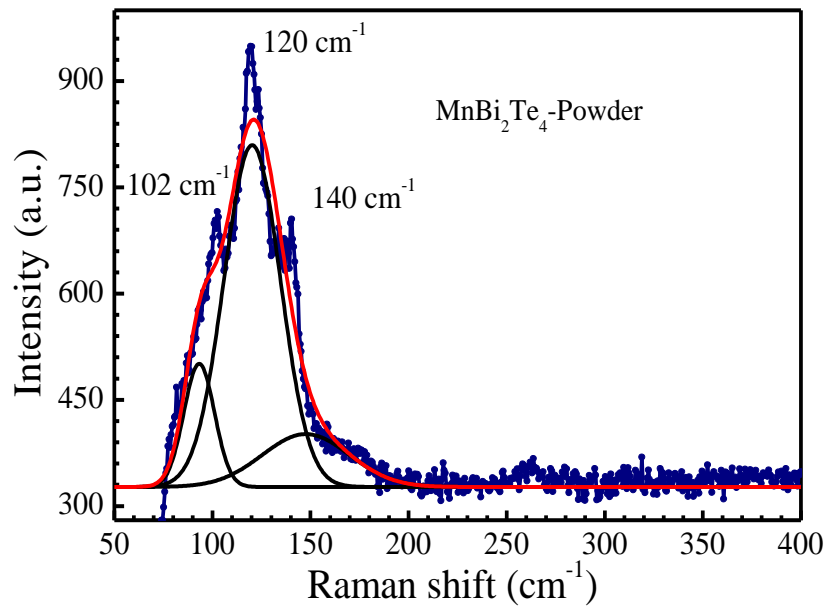


Fig. 7

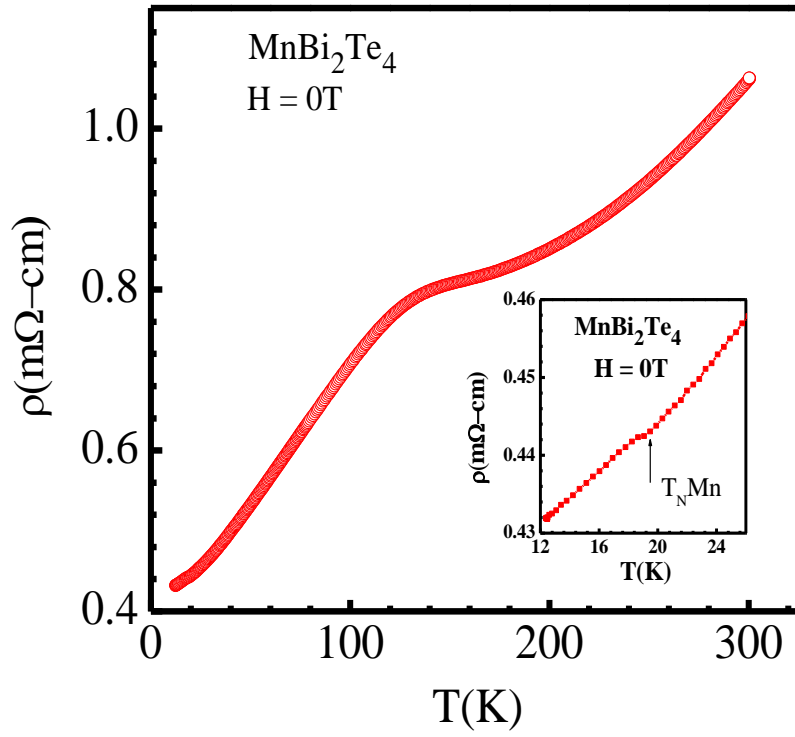


Fig. 8

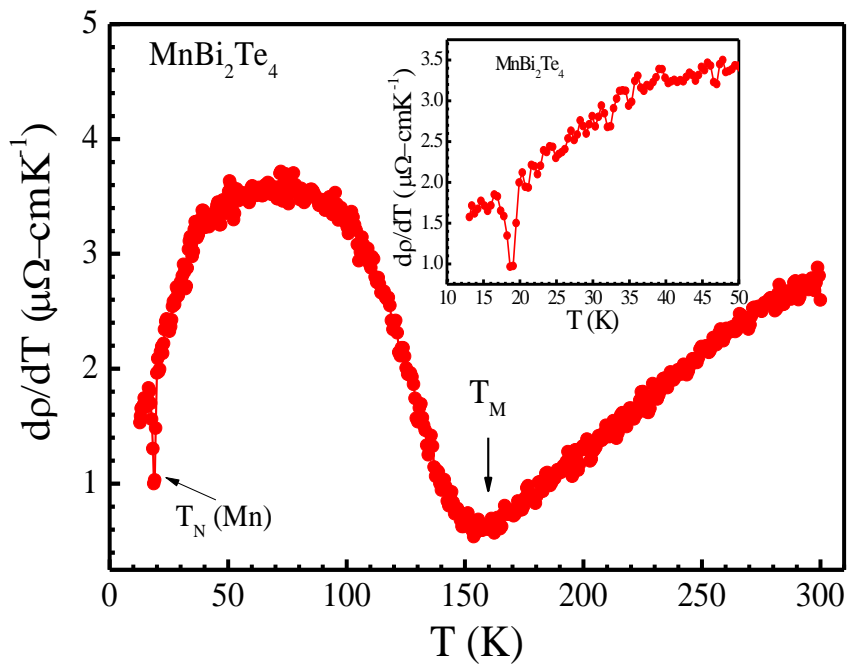


Fig. 9

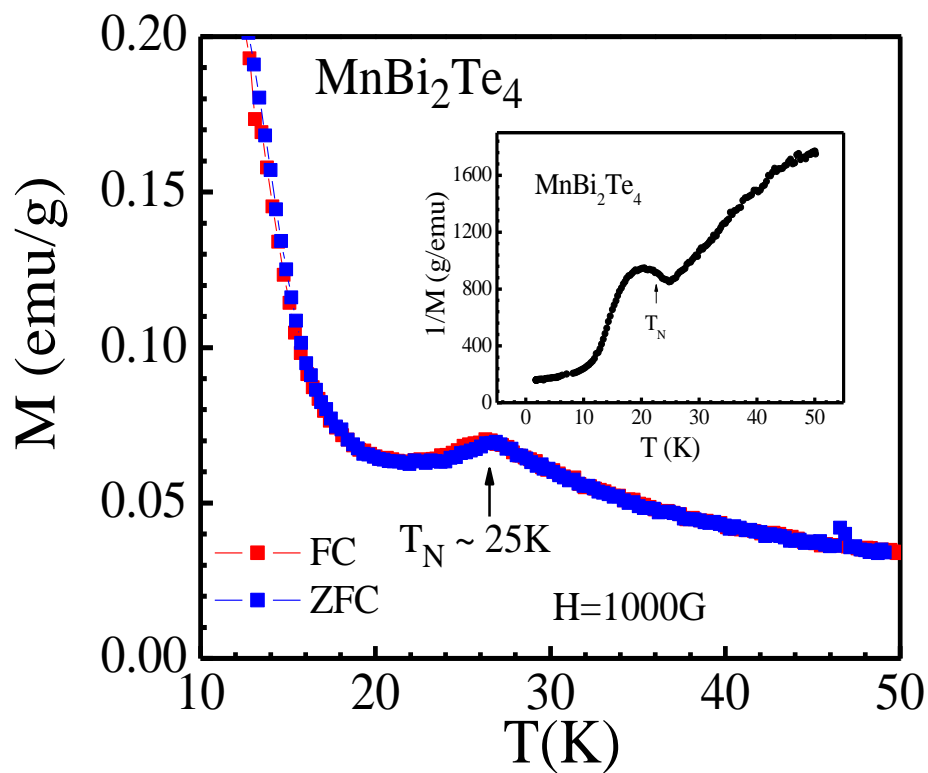


Fig. 10

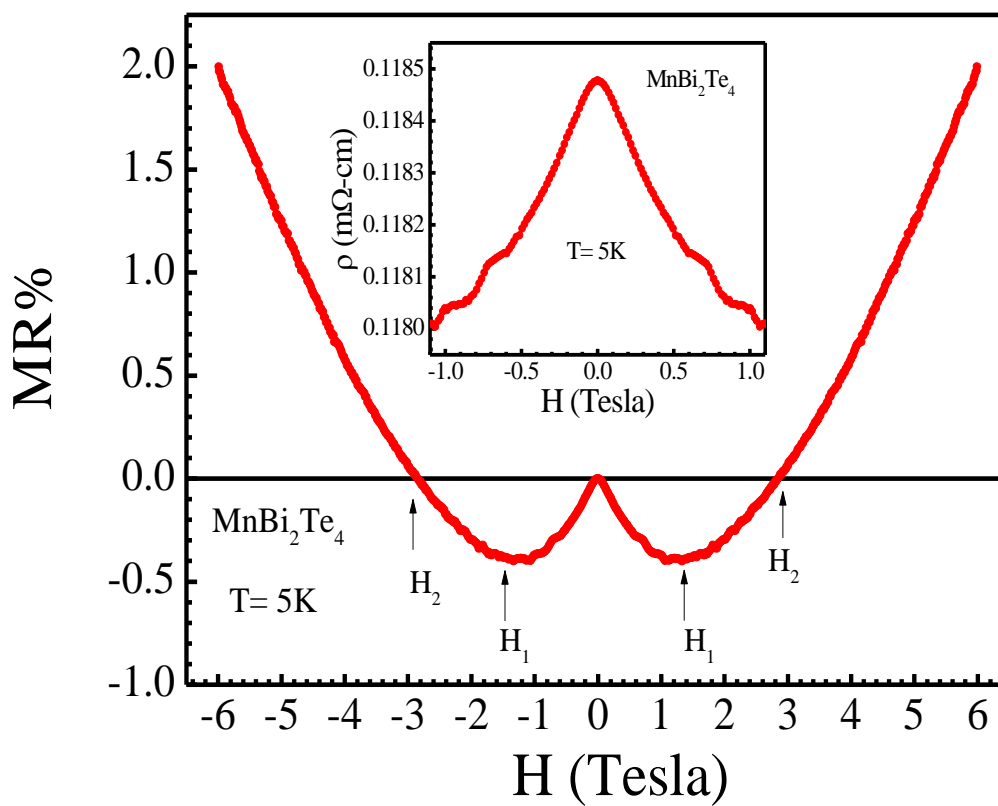


Fig. 11